Journal of
Renewable Energy Research and Applications (RERA)

Vol. 5, No. 1, 2024, 93-106 *DOI: 10.22044/rera.2023.12861.1207*

Numerical Investigation of Effect of Fin Geometry on Melting Process of Phase Change Material in an Evacuated Tube Solar Collector

S. Y. Afshoon, R. Shafaghat* and M. Gorji Bandpy

Sea-Based Energy Research Group, Babol Noshirvani University of Technology, Babol, Iran.

Received Date 19 March 2023; Revised Date 13 April 2023; Accepted Date 15 April 2023
**Corresponding author: rshafaghat@nit.ac.ir (R. Shafaghat)*

Abstract

This work investigates the melting behavior of phase-change material (PCM) in an evacuated tube solar collector. The outer tube is made of borosilicate glass with a diameter of 60 mm, and the inner tube is made of copper with a diameter of 10 mm and length of 1500 mm. The heat transfer problem in heat pipe is investigated in four cases: finless, full fin, half fin, and third fin. The fins are cut from a 35 mm diameter copper tube and installed concentrically with the outer tube. The inner space between the absorber tube and the heat pipe is filled with stearic acid as the PCM. The numerical simulation is conducted using the Ansys Fluent 2022 for the laminar incompressible Newtonian fluid flow in the transient state via the enthalpy-porosity model. The initial temperature of PCM is 27 ˚C, and liquid fraction is zero at the beginning of the simulation. After validating the numerical results with the experimental ones, the collector performance is evaluated by considering the four temperatures of 68, 72, 76, and 80 ˚C for the fin and heat pipe at the three different times t = 22, 55, and 110 s. The results show that by increasing the fin area in the three cases of third fin, half fin, and full fin, the melting and storage time of PCM are reduced by 6%, 44%, and 87%, respectively. Also as the Estefan number increases from 0.007 to 0.05, 0.09, and 0.13, and the process of PCM melting decreases by 75%, 85%, and 92%, respectively.

Keywords: *PCM, Fin, Thermal Conduction, Natural Convection, Enthalpy-Porosity.*

1. Introduction

Using new energy sources and innovating new methods for decreasing energy consumption is always important. The hot water demand in daily life and different industries has significantly increased due to the growth of the population and industry. Due to the energy crisis and high cost of fossil fuels on the one hand, and unreliable nuclear power plants on the other, the use of renewable and inexpensive energies has been expanded [1]. Solar energy is the most exclusive energy source in the world, which can be converted to other forms of energy directly and indirectly [2]. Despite the numerous benefits of solar energy, the important issue is that the sun is not always available; therefore, most solar energy conversion systems are required to use heat storage systems. Using energy storage systems improves the performance and reliability, and decreases energy consumption [1].

One of the new and efficient methods in the field of thermal energy storage is the use of PCMs. Many studies have been conducted on applying PCMs in solar collectors and heat exchangers. In an experimental study, Medrano *et al*. [3] investigated the heat transfer properties of five heat exchangers including a double-pipe heat exchanger with PCM in the annular space, a double-pipe heat exchanger with PCM in the graphite matrix space, a double-pipe heat exchanger with PCM in the outer fin space on copper tubes, a coil heat exchanger having compact fins with PCM in the space between the coil and fin, and a plate heat exchanger with PCM in the half of the space through which the fluid passes, as energy storage systems. Their results indicated that the double-pipe heat exchanger with PCM in the annular space has a higher thermal performance. In another experimental study, Huang *et al*. [4] found that when the evacuated-tube solar collector is equipped with fins, the thermal efficiency improves by 11.8%. Feliński *et al*. [5] found that the efficiency of annually charging the evacuated-tube solar collector with paraffin as the PCM is between 33% to 66% compared with the evacuated-tube solar collector without PCM. Abokersh *et al*. [6] observed that

the thermal efficiency of the evacuated tube collector with paraffin injection as the PCM is higher than the ETC without PCM by 14%. Also they revealed that the thermal efficiency of PCM-injected solar collectors with and without fins is greater than that of solar collectors without PCM by 35.8% and 47.7%, respectively. Xue *et al*. [7] used barium hydroxide octahydrate ($Ba(OH)_2.8H_2O$) as an energy storage material to enhance both the daily and average thermal efficiency of the U-shaped tube in the ETC system. Naghavi *et al*. [8] observed that the thermal performance of ETC with a heat pipe after PCM injection is higher than a collector with similar characteristics but without PCM. Papadimitratos *et al*. [9] investigated the thermal performance of ETC with two different PCMs (tritriacontane and erythritol), and found that the thermal efficiency of the proposed system improved by 26% and 66%, respectively, relative to the ETC system without PCM. In another experimental study, Felinski and Sekret [10] used paraffin wax as an integrated PCM in ETC with a combined parabolic concentrator (CPC). They observed that the maximum and average charge efficiency of the ETC system improved from 40% to 49% and from 31% to 36%, respectively. Li and Zhai [11] evaluated the thermal performance of ETC with graphite and erythritol as combined PCM. According to the results, when solar radiation intensity was 12.88 MJ/m^2, the heat storage rate and average storage efficiency of the proposed system with PCM were equal to 5.17 MJ/m^2 and 40.17%, respectively. Naghavi *et al*. [12] experimentally evaluated the heat pipe performance in an ETC with paraffin as a latent heat storage material. It was reported that the efficiency of the proposed system in rainy-cloudy and sunny days varied between 34% and 36% and 38% and 42%, respectively. Also it was observed that changing the water flow rate directly affects the efficiency of the proposed system. Essa *et al*. [13] found that the energy efficiency of ETC is lower by 21.9% compared to ETC combined with paraffin wax as the PCM when the water flow rate has the lowest value. It was observed that an increase in the thermal efficiency of the ETC system with the PCM is due to the complete phase change of the PCM. At the highest flow rate with 1.2 L/min, the daily efficiency of the PCM integrated in the collector reached 6.8%. Bazri *et al*. [14] reported that the energy efficiency of the system extended with three types of PCM was in the range of 36-54%, and the thermal efficiency during rainy-cloudy days improved to the range of 47-58%. Moreover, simulation results indicated that the thermal efficiency of an extended solar collector was higher than a conventional collector, even when working under weak solar radiation and low ambient temperature. Rahimi *et al*. [15] experimentally studied the melting/solidification process of PCM in a fin and tube heat exchanger. The effects of different fluid parameters including the inlet fluid flow rate and temperature were analyzed. Brent *et al*. [16] utilized enthalpy-porosity to calculate the position of the solidification front. In this method, a porous region with a mixture of liquid and solid particles was created by considering the plastic region in the impure PCM due to the difference between melting and solidification temperatures. The concept of the porous medium and permeability was considered in the interface of two phases. The comparison of the numerical results in this study with the experimental results of Gallium melting shows the acceptable performance of the proposed method. Seddegh *et al*. [17] investigated the effects of free convection in a double-pipe concentric heat exchanger using the enthalpy-porosity technique in horizontal and vertical arrangements. Lacroix [18] investigated the transient behavior of a latent heat storage unit in an analytical study. In this study, it was indicated that the thermal and geometric parameters significantly affect the improved thermal performance of the system. Aghaei *et al*. [19] investigated the effect of the eccentricity of the inner tube on the melting/solidification processes of PCMs in a double-pipe horizontal heat exchanger considering the effects of natural convection. For this purpose, the eccentricity was downward in the melting process and upward in the solidification process. Seeniraj *et al*. [20] investigated the thermal behavior of a high-temperature PCM stored in shell and tube heat exchangers. It was observed that if a finless tube is used, a fraction of PCM remains solid near the tube outlet because the difference between the inlet fluid temperature and the melting point of the PCM is very low in the proximity of the tube outlet. Also it was reported that in the presence of some radial fins, there was further temperature difference between the fluid temperature and the melting point of the PCM. Additionally, further melting was observed in the axial direction. Dhaidan *et al*. [21] experimentally and numerically investigated the PCM melting process using nanoparticles in a shell and tube heat exchanger under constant heat flux with a geometric condition of increasing eccentricity. Arshad *et al*. [22] experimentally investigated the performance of heat well with needle fins using n-

ecosine and paraffin wax as phase change material in 4 different configurations. They also investigated the volume fraction of the phase change material, and the results showed that ecosin and paraffin had the best thermal performance in thicknesses of 2 and 3 mm, respectively. Rostamian *et al*. [23] investigated the effect of constant and intermittent electric power changes in different volume fractions of 11, 25, and 50% stearic acid as PCM on board temperature changes. The results showed that an 11% volume fraction of PCM at a power of 4 watts increased the safe operating time by 20 minutes. By Rahimi *et al*. [24], numerical simulation of the melting process of phase change material in a shell and tube heat exchanger in the presence of different types of radial fins was investigated. The results showed that the higher the penetration of the fin in the lower half of the shell, the melting will improve in the final times, and the complete melting time will decrease. Alshukri *et al*. [25] investigated a new method experimentally; the incorporation of phase change material (PCM) in one or both of the discharge tubes (ET) and two separate tanks adjacent to the collector water tank of a heat pipe evacuated tube solar water heater (HP/ETC). In this method, the evacuated tube was filled with medical paraffin wax as thermal heat storage, while two separate reservoirs were filled with paraffin wax (gradeA). The results showed that the incorporation of PCM in both ET and isolated tanks improved the efficiency by 55.7%, while the incorporation of PCM in ET led to an increase in efficiency of 49.9%, and the efficiency with the incorporation of PCM in isolated tanks was about 36.5% compared to without. PCM improved. Chuanhui Zhu. [26], considering the problems of low utilization rate of solar heat in mountainous areas of solar energy, an air-type vacuum tube solar collector (AVSC) with air as the heat exchange medium was designed and investigated. The solar heat collector vacuum tube adopted a two-pass spiral direct flow structure, and the vacuum tube had an internal heat storage rod. The results showed that the average heat collection efficiency of the vacuum tube solar collector without phase change heat storage rods was 38%. The evacuated tube solar collector using water as the heat transfer medium had an average heat collection efficiency of 58%. The average heat collection efficiency of the equivalent AVSC with internal phase change heat storage rod was 61%. Amr Elbrashy *et al*. [27]

ETSC integrated with nano-enhancer phase change material (NE-PCM). To achieve this purpose, a system consisting of 5 linked collecting panels was designed, fabricated, and experimentally investigated. Each panel included a glass-evacuated tube with two concentric aluminum pipes installed inside. NE-PCM was placed between the inlet and outlet air paths inside the evacuated tube to enhance the heat transfer rate. The performance was investigated with and without NE-PCM at five mass flow rates (0.006, 0.008, 0.01, 0.03, and 0.05 kg/s). Experimental results revealed that the highest temperature was 116,108, 102, 95, and 93 ˚C, respectively, for the above mass flow rates without adding NE-PCM. The outlet temperature was decreased by 6–15 ˚C when using NE-PCM. The SAH efficiency was increased by 29.62% compared to the system without NE-PCM at 0.05 kg/s. The maximum thermal efficiency for the system with NE-PCM was 62.66% at 0.05 kg/s.

The purpose of this study is to investigate the role of using fin and increasing the area of the coaxial fin with the absorber tube in the conductive heat transfer structure and its effect on the melting rate of the phase change material. The use of stearlic acid as a phase change material, which due to its high melting temperature and direct effect on the latent heat of melting, increases the amount of thermal energy storage, and finally, more hot water can be used in non-sunny hours. The melting and storage time of the stearlic acid phase change material is reduced by increasing the fin area from 87% to 92% compared to the heat pipe without fins.

The results of this study indicate that increasing the nanoparticle content and eccentricity directly affect the fraction of molten PCM. The above review of previous studies indicates that fin geometry significantly affects the performance of an evacuated tube solar collector. In addition, depending on the geographical location, employing a PCM and an energy storage are important issues for increasing the efficiency of the evacuated tube solar collectors. Hence, this study numerically investigated the effect of changing the fin geometry in the presence of stearic acid as a PCM. The fin geometry was selected with a comprehensive viewpoint to effectively perform during the day as the solar irradiance angle was altered. The fin was installed concentrically with the solar collector and eccentric heat pipe.

2. Problem statement

This study used the small-scale solar collector model for dimensionless parameters' numerical simulations. Hence, table 1 presents the geometry

and dimensions of the solar collector and its components in both original and model scales.

Table 1. Dimensions of the original and small-scaled collector.

Original collector		Small-scaled collector	
Absorber tube diameter	60 mm	Absorber tube diameter	5.2 mm
Heat pipe diameter	10 mm	Heat pipe diameter	0.85mm
Full fin diameter	35 mm	Full fin diameter	3 mm
Distance of cut area from the bottom of the fin	10 mm	Distance of cut area from the bottom of the fin	0.85 mm
Fin thickness	1.5 mm	Fin thickness	0.13 mm
Collector length	1500mm	Collector length	1500 mm

The general schematic of the physical model is presented in figure 1. The solar collector consisted of an adiabatic outer tube made from borosilicate glass, and an inner tube or heat pipe made from copper. Fins connected to the heat pipe improve the heat transfer rate.

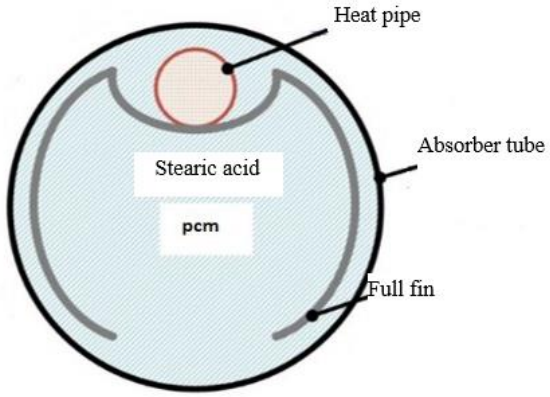

Figure 1. Physical schematic of simulated domain filled with PCM.

Simulations were conducted for three cases with fins and one without a fin (Figure 2). The fins were made from copper and evaluated in the three cases of full fin, half fin, and third fin.

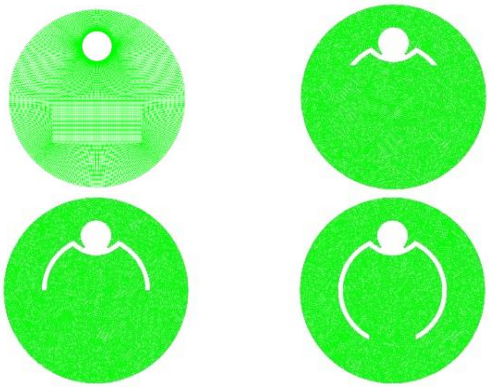

Figure 2. Physical schematic of fin geometry and mesh generation.

The inner space between the absorber tube and heat pipe was filled with stearic acid as the PCM. The 100% acetone with nanographene was considered as the working nanofluid in the heat pipe.

Regarding the typical performance of the solar collector, the heat was transferred to the PCM and fins through the radiation heat transfer mechanism, then the heat was transferred from the heat pipe to the nanofluid. In order to examine the performance of the fins, evaluations were performed at the four temperatures of 68, 72, 76, and 80 ˚C in the heat pipe containing acetone-graphene nanofluid. Heat was assumed to be inversely transferred from the heat pipe to the fins, and the initial temperature of PCM was 27 ˚C. The adiabatic boundary condition was applied to the outer tube walls.

3. Non-dimensionialization

Regarding the dimensions of the solar collector, numerical simulations were conducted on a small-scale model. For this purpose, the proper dimensionless parameters were obtained using the Buckingham π theorem, considering the equations of the melting and solidification processes. In both processes, the convection heat transfer coefficient can be defined as follows:

$$\mathbf{h} = \mathbf{h}\left(\Delta\mathbf{T}, \mathbf{g}(\boldsymbol{\rho}_\mathbf{s} - \boldsymbol{\rho}_\mathbf{l}), \mathbf{h}_\mathbf{s}, \boldsymbol{\sigma}, \mathbf{l}, \boldsymbol{\rho}, \mathbf{c}_\mathbf{p}, \mathbf{k}, \boldsymbol{\mu}\right) \quad (1)$$

where $\Delta T = |T_S - T_{sat}|$ is the difference between the surface temperature (T_s) and saturation temperature (T_{sat}), $g(\rho_s - \rho_l)$ is the body force due to the liquid-solid density difference, h_s is the latent heat of melting, σ is the surface tension, L is the characteristic length, and ρ, C_P, K, and μ are the thermophysical properties of PCM in the liquid or solid phase. The dimensionless groups obtained from Buckingham π theorem (like [28]) are presented in equations (2) and (3) [29].

$$\frac{\mathbf{hl}}{\mathbf{k}} = \mathbf{f}\left(\frac{\boldsymbol{\rho}\mathbf{g}(\boldsymbol{\rho}_\mathbf{s} - \boldsymbol{\rho}_\mathbf{l})\mathbf{l}^\mathbf{3}}{\boldsymbol{\mu}^\mathbf{2}}, \frac{\mathbf{c}_\mathbf{p}\Delta\mathbf{T}}{\mathbf{h}_\mathbf{s}}, \frac{\boldsymbol{\mu}\mathbf{c}_\mathbf{p}}{\mathbf{k}}, \frac{\mathbf{g}(\boldsymbol{\rho}_\mathbf{s} - \boldsymbol{\rho}_\mathbf{l})\mathbf{l}^\mathbf{2}}{\boldsymbol{\mu}}\right) \quad (2)$$

$$\mathbf{Nu}_\mathbf{l} = \mathbf{f}\left(\frac{\boldsymbol{\rho}\mathbf{g}(\boldsymbol{\rho}_\mathbf{s} - \boldsymbol{\rho}_\mathbf{l})\mathbf{l}^\mathbf{3}}{\boldsymbol{\mu}^\mathbf{2}}, \mathbf{ja}, \mathbf{pr}, \mathbf{Bo}\right) \quad (3)$$

$$\mathbf{Gr}_\mathbf{l} = \frac{\mathbf{g}\boldsymbol{\beta}(\mathbf{T}_\mathbf{s} - \mathbf{T}_\infty)\mathbf{l}^\mathbf{3}}{\boldsymbol{\nu}^\mathbf{2}} \quad (4)$$

where Nu_l is the Nusselt number, ja is the Jacob or Stefan number (ratio of heat required for temperature alteration to the latent heat), ΔT is the temperature difference between liquid and solid phases of the PCM., Pr is the Prandtl number, Bo is the Bond number (ratio between the gravitational forces and surface tension forces), and Gr_l is the Grashof number. In the Grashof relationship, β is the volumetric expansion coefficient, defined as the ratio between the fluid

density change and temperature difference at the constant pressure [29].

$$\boldsymbol{\beta = -\frac{1}{\rho}\left(\frac{\partial \rho}{\partial T}\right)_P = -\frac{1}{\rho}\left(\frac{\rho_\infty - \rho}{T_\infty - T}\right)} \quad (5)$$

If the variation of ρ in numerical simulations is considered by Boussinesq approximation (Equation (6)), the volumetric expansion coefficient will be activated [29].

$$\boldsymbol{\rho_\infty - \rho \cong \rho\beta(T - T_\infty)} \quad (6)$$

4. Governing equations

For simplifying physical and mathematical equations governing the problem, the following assumptions are considered:

- The fluid flow is 2D, laminar, and unsteady.
- The molten material behaves like an incompressible Newtonian fluid.
- Viscosity losses in the heat transfer process are insignificant.
- The absorber tube or the same outer tube is made from glass, and is adiabatic with negligible heat dissipation.
- The thermal resistance of the inner tube or the same heat pipe is negligible.
- Thermo-physical properties of the heat-transfer fluid and PCM are constant.
- The volumetric changes due to phase change and longitudinal effects are ignored.
- The outer wall temperature of the inner tube is equal to that of the fins, and is constant.
- Heat is transferred in the PCM through conduction and free convection mechanisms.

The properties of the PCM (stearic acid commercially named SA-67 with the chemical composition of C18H36O2) are presented in table 2.

The enthalpy-porosity method models the phase change process [16]. This method uses a static grid, and the governing equations are modified to be valid in both phases. In this case, there is no need to determine the interface position. The governing equations were solved in the entire grid simultaneously, and the molten PCM fraction was computed in each iteration. The plastic region is where the porosity increases from 0 to 1 as the PCM melts. When a region freezes completely, the porosity becomes zero, and the flow velocity decreases to zero in this region. When the PCM has melted completely, the liquid fraction is 1; when it is solid, it is 0. As time passes, the liquid fraction is between 0 and 1. In phase change problems, governing equations include continuity, momentum, and energy [1, 24, 31].

Table 2. Properties of stearic acid as PCM [30].

Thermo-physical properties of stearic acid	
Level of purity	99.92%
Latent heat (heat storage capacity)	244.21 (J/g)
Melting point	67.3 (˚C)
Solidification point	66.1 (˚C)
Density (@ 40 ˚C)	1.10 (g/cm^3)
Density (@ 80 ˚C)	1.19 (g/cm^3)
Specific heat capacity (@ 40 ˚C)	2.01 (kj/kg.k)
Specific heat capacity (@ 80 ˚C)	2.47 (kj/kg.k)
Volumetric expansion coefficient	0.0008 (k^{-1})
Kinematic viscosity	1.5×10^5 (m^2/s)
Thermal conductivity	0.17-0.29 (W/m.k)

$$\boldsymbol{\nabla . \vec{v} = 0} \quad (7)$$

$$\boldsymbol{\frac{\partial V}{\partial t} + \vec{v}.\nabla\vec{v} = \frac{1}{\rho}\left(-\nabla P + \mu\nabla^2\vec{V} + \rho\vec{g}\beta(T - T_{ref})\right) + \vec{s}} \quad (8)$$

$$\boldsymbol{\frac{\partial h}{\partial t} + \frac{\partial H}{\partial t} + \nabla.\left(\vec{V}h\right) = \nabla.\left(\frac{k}{\rho C_p}\nabla h\right)} \quad (9)$$

The total enthalpy of the material is the sum of sensible enthalpy h and latent heat ΔH (Equation (10)) [1, 24, 31].

$$\boldsymbol{h = h_{ref} + \int_{T_{ref}}^{T} C_p\, dt} \quad (10)$$

Equation (11) gives the latent heat [1, 24, 31]:

$$\boldsymbol{\Delta H = \beta . L_H} \quad (11)$$

ΔH may vary from zero (solid phase) to 1 (liquid phase). For this purpose, the volume fraction of molten PCM (β) in equation (11) is defined by equations (12), (13), and (14) [1, 24, 31]:

$$\boldsymbol{\beta = \frac{\Delta H}{L_H} = 0 \quad if \ (T < T_S)} \quad \text{Solidification state} \quad (12)$$

$$\boldsymbol{\beta = \frac{\Delta H}{L_H} = 1 \quad if \ (T > T_l)} \quad \text{Melting state} \quad (13)$$

$$\boldsymbol{\beta = \frac{\Delta H}{L_H} = \frac{T - T_{solidus}}{T_{liquidus} - T_{solidus}} \quad if \quad T_s < T < T_l} \quad \text{Plastic state (phase change boundary)} \quad (14)$$

Equation (15) gives the total enthalpy [1, 24, 31]:

$$\mathbf{H = h + \Delta H} \quad (15)$$

In the above equations, T_s and T_l denote the initial and final temperatures in the melting region of PCM. Also in equation (8), S is the source term, which is added to the momentum equation in the convection heat transfer due to phase change effects (Equation (16)) [1, 24, 31].

$$\mathbf{S} = \frac{\mathbf{A_{mush}(1-\beta)^2}}{\boldsymbol{\beta^3 + \varepsilon}} \quad (16)$$

where A_{mush} denotes the plastic region constant, which varies between 10^4 and 10^7. Values higher than this constant represent the steeper slope of velocity reduction, and very high values of this constant may create fluctuations in the solution. In this study, the plastic region constant was assumed to be 10^5. $\varepsilon = 0.001$, which is a small value that avoids the issue of the denominator of the source term fraction being zero. Finally, the initial temperature was considered $T_{ref} = 300.15\ K$.

5. Numerical simulation

5.1 Numerical method

This study numerically simulates the PCM melting process using the finite volume method in the environment of Ansys Fluent 2022. This simulation was performed in the 2D state transiently using the enthalpy-porosity model, and the laminar flow regime and incompressible Newtonian fluid are assumed. The simple algorithm was used for pressure-velocity coupling, the presto method was used for the pressure term, and the second-order upwind method was used for momentum and energy equations. Relaxation factors for velocity components, pressure correction, heat energy, and liquid fraction are considered 0.7, 0.3, 0.9, and 0.9, respectively. In addition, the time step for the simulation was selected as 0.1 s. The convergence criteria or solution accuracy was assumed to be 10^{-3} for the continuity equation and 10^{-6} for the momentum and energy equations [32, 33].

5.2 Grid independence

Examining the grid independence of numerical solutions is necessary for determining the optimal time step and element size in simulations. Four different grids with 45000, 50000, 54000, and 58000 cells were considered for evaluating the grid independence. The simulations were conducted by selecting the half-fin geometry at 68 °C (Figure 3). The evaluations indicate that the grid with 54000 cells was the final grid for performing computations because, as the number of computational cells increases to 58000, the relative error would be lower than 0.5. Then for determining the proper time step, the five time steps of 0.01, 0.05, 0.1, 0.5, and 1 s were examined (Figure 4). Regarding the conducted evaluations, a time step of 0.1 s was selected for the simulations.

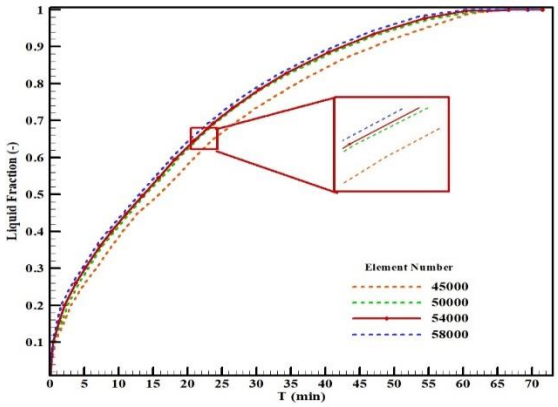

Figure 3. Grid independence results.

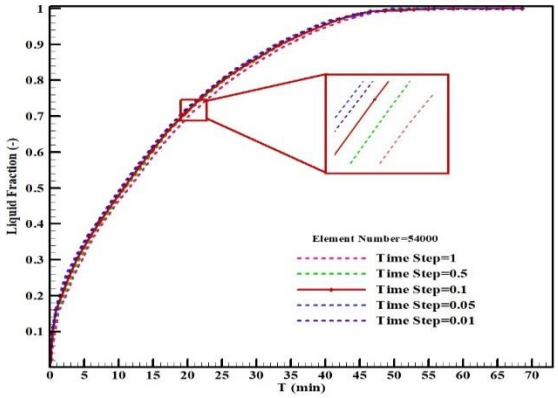

Figure 4. Time step independence results.

Figures 5 and 6 present the unstructured mesh generated on the heat pipe and fin surface, along with standard skewness and orthogonal quality plots. As illustrated in the figures, the standard skewness of more than 95% of the elements tends toward zero, and the orthogonal quality of more than 95% of elements tends toward 1.

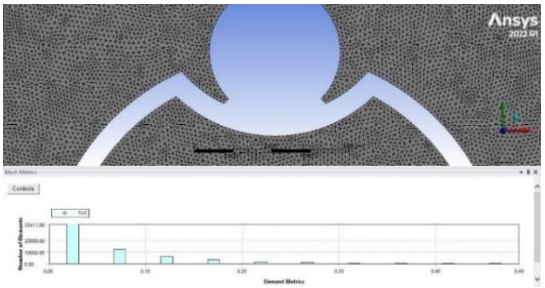

Figure 5. Sample mesh generated on the geometry with full fin along with standard skewness plot.

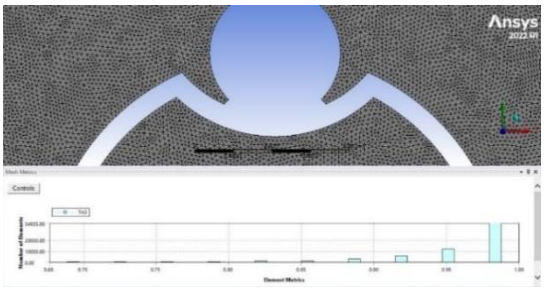

Figure 6. Sample mesh generated on the geometry with full fin along with the orthogonal quality plot.

5.3 Validation method

For validating the numerical results, the PCM behavior in a spherical capsule with a diameter of 101.66 mm and thickness of 1.5 mm was investigated experimentally and numerically (Figure 7). The capsule space was spherical and made from transparent glass, which was filled with paraffin n-octadecane as the PCM. Sensor E was located in the center of the sphere, points A, B, C, and D were located beneath the sensor, and points H, G, and F were located above sensor E. Therefore, the distances EF, FG, and GH between the sensors above the center were +12.5 mm, the distances ED, DC, and CB between the sensors under the center were -12.5 mm symmetrically relative to the center of the sphere (point E). The EA distance was equal to -44 mm from the center of sphere along the vertical axis. Sensors K, I, and J were along the horizontal axis, and were used for monitoring the temperatures of the inner and outer surfaces of the sphere. The EK distance was +44 mm, and the EJ distance was -44 mm symmetrically relative to the sphere's center. The validation of this analysis was conducted experimentally and numerically, and the PCM melting temperature was 28.2 ˚C [25].

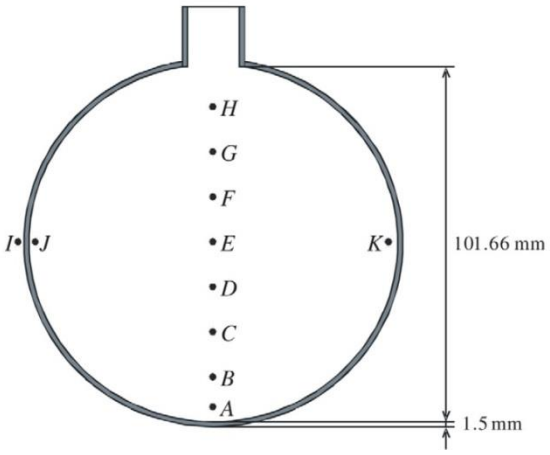

Figure 7. Geometry of the spherical capsule with PCM-filled simulation domain presenting the positions of the thermal sensors [25].

Initially, the capsule was filled with liquid PCM, and then the PCM inside the capsule was solidified by placing the capsule in a cold water bath at a temperature of 27.2 ˚C. Then for evaluating the phase change process, the spherical capsule was placed in an insulated hot water enclosure, and the surface temperature of the sphere was maintained at 40 ˚C. The results of the simulations in the present study have been compared with the numerical and experimental results presented by Tan *et al*. [25] (Figure 8). As it can be seen, the numerical results in the present study agree with the numerical results of Tan *et al*. [25].

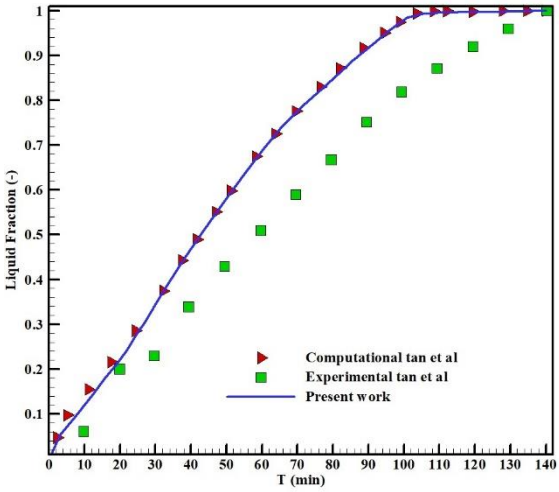

Figure 8. Comparison of the validation diagram of liquid fraction versus time between the present study and Tan *et al*. [34].

6. Results and discussion

Initially, the fin geometry and inlet temperature on the PCM were investigated. The variation of liquid fraction against time (in minutes) is presented for the four geometries of heat pipe without fin, with full fin, with half fin, and with third fin, respectively, in figures 9 to 12.

The results indicate that fin presence with different arrangements, in comparison to the case without fin, significantly affects the melting process of PCM. In addition, adding fins to the heat pipe decreases the melting time of the PCM, while also extending the surface area; the more extended the fin surface, the faster the PCM melting process due to a higher heat transfer rate. As illustrated in table 3, the melting time of the PCM in different finned geometries was reduced compared to the finless geometry. The highest melting time (128 minutes) was found to be related to the finless case at inlet temperature of 68 ˚C, while the lowest melting time (2 minutes) was related to the finned pipe with full fins at an

inlet temperature of 80 ˚C. In addition, the melting time of the PCM in the finless, third fin, half fin, and full fin cases at a constant temperature of 72 ˚C was equal to 37, 35, 20, and 4 minutes, respectively. This significant reduction in melting time can be argued to be due to the presence of the fins and how the surface area is extended. The PCM melting time for different geometries and temperatures is presented in table 3.

Table 3. PCM melting time at different temperatures.

PCM melting time in minutes for 4 geometries at 4 different temperatures				
Temperature/geometry	Finless	third fin	half fin	Full fin
68	128	121	72	20
72	37	35	20	4
76	21	20	12	3
80	16	15	9	2

Since the fin surface is coaxial with the collector surface, for more extended surface areas, the PCM melting time considerably decreases by significantly increasing the heat flux absorption at different times of the day. Therefore, compared to the finless case, in the full fin, half fin, and third fin cases, the PCM melting time decreased by 87%, 44%, and 6%, respectively, at temperatures of 68, 72, 76, and 80 ˚C. Additionally, the results confirm that increasing the fin surface area amplifies the free convection mechanism, and the melting process is accelerated at the final times of the process simultaneously with the desired effect of the heat conduction mechanism. Also because of the difference in the melting temperature, the higher the surface temperature of the heat pipe surface, the lower the melting time of the PCM. In the present study, a decrease in the melting time at 80 ˚C was clearly observed relative to 68 ˚C, 72 ˚C, and 76 ˚C.

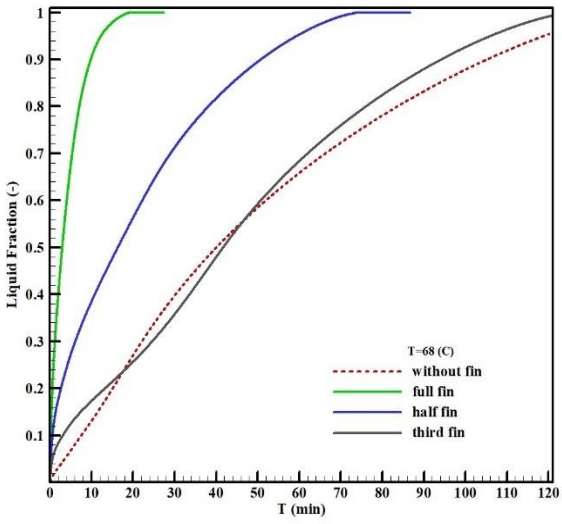

Figure 9. Liquid fraction versus time at 68 ˚C.

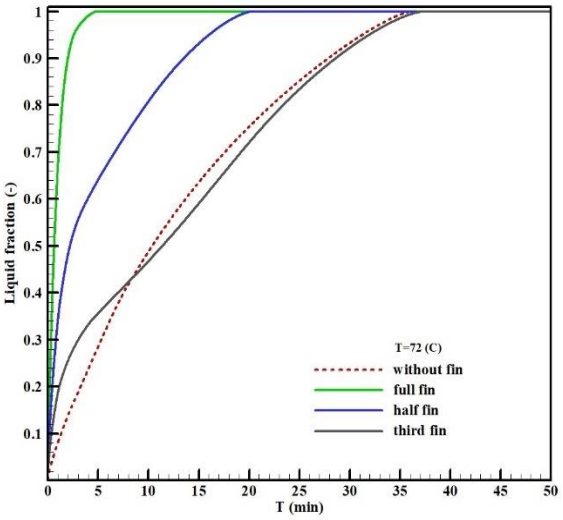

Figure 10. Liquid fraction versus time at 72 ˚C.

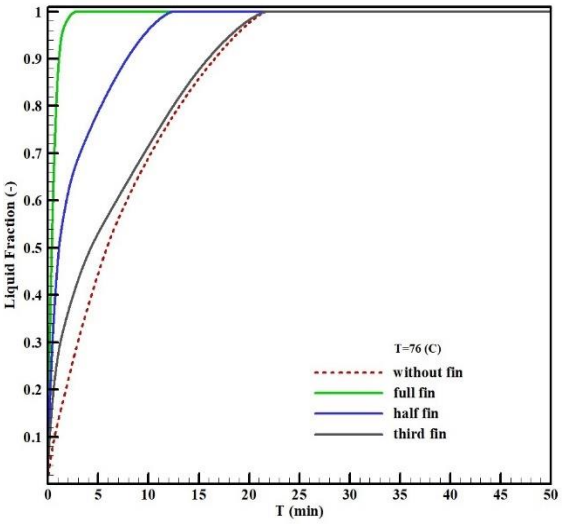

Figure 11. Liquid fraction versus time at 76 ˚C.

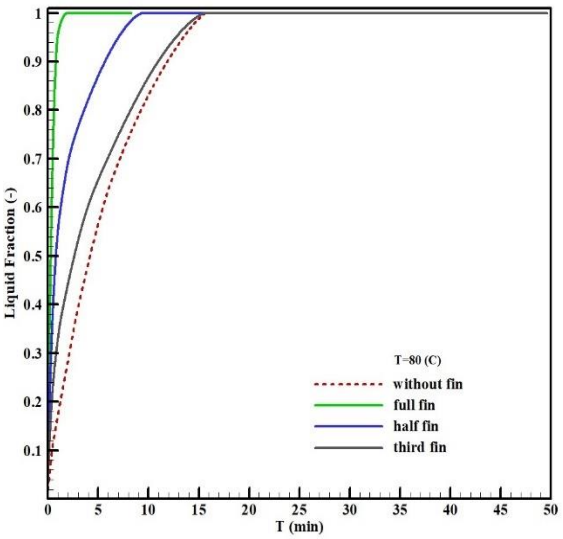

Figure 12. Liquid fraction versus time at 80 ˚C.

PCM temperature variation with time (in minutes) for the temperatures of 68 ˚C, 72 ˚C, 76 ˚C, and 80 ˚C in the four geometries of without fin, with full fin, with half fin, and with the third fin is

presented in figures 13 to 16. The results indicate a more rapid rise of the PCM temperature as the heat pipe's wall temperature increases. Increasing the fin surface area, one-third fin, half fin, and full fin, compared to the finless geometry, significantly increases the melting process progression regarding the surface temperature of the heat pipe wall. A comparison of temperature variation with time in the finless and finned geometries shows that the melting process initiated from the surrounding of the heat pipe, and the melting trend was the same for finless and finned cases. However, as the melting process progressed, the positive effects of the fins were revealed when the heat transfer mechanism converted from conduction to natural convection. It is worth mentioning that the four considered temperatures (68 ˚C, 72 ˚C, 76 ˚C, and 80 ˚C) are equivalent to the four Stefan numbers of 0.007, 0.05, 0.09, and 0.13, respectively; hence, the collector had the best performance at maximum Stefan number.

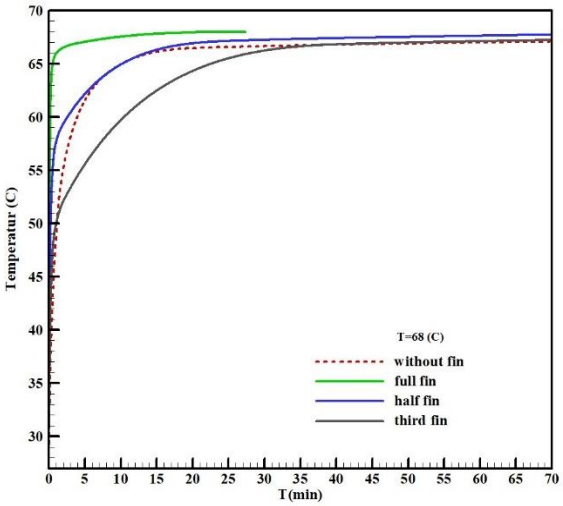

Figure 13. Temperature variation against time at 68 ˚C.

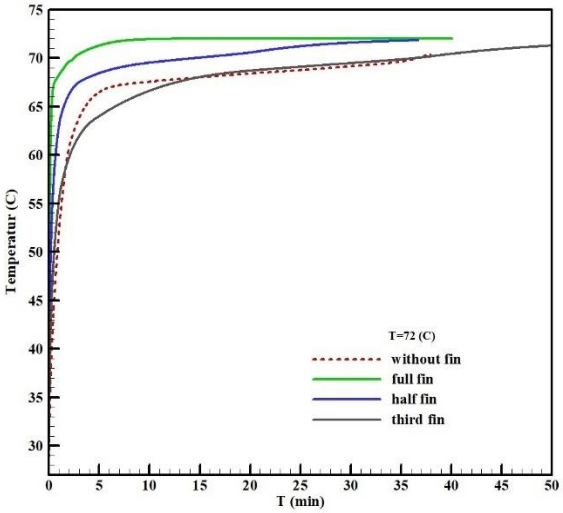

Figure 14. Temperature variation against time at 72 ˚C.

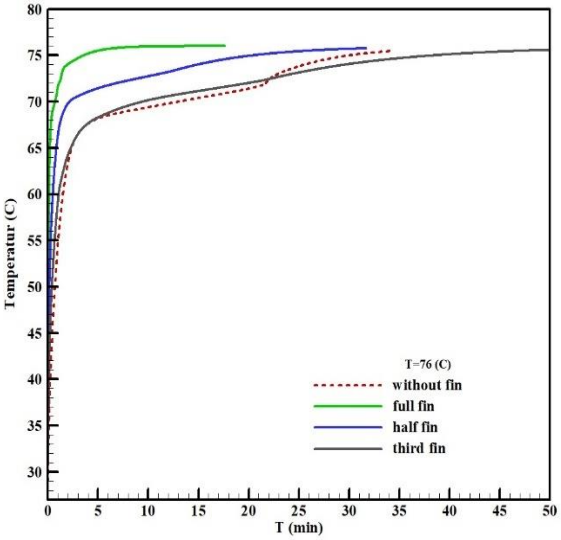

Figure 15. Temperature variation against time at 76 ˚C.

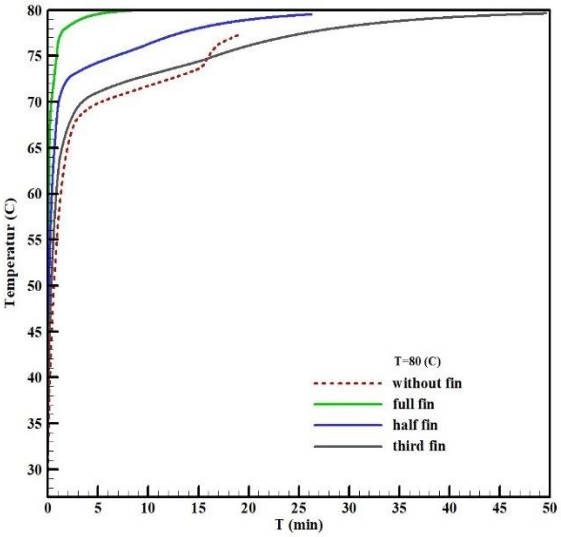

Figure 16. Temperature variation against time at 80 ˚C.

In this section, the liquid fraction, temperature, and velocity contours at the temperatures of 68 ˚C, 72 ˚C, 76 ˚C, and 80 ˚C for the four without fin, with full fin, with half fin, and with third fin geometries at different times are presented in figures 17 to 28. A value of 1 denotes the complete liquid phase, and a value of 0 denotes the complete solid phase. At the beginning of the process, heat was transferred from the hot wall via the conduction heat transfer mechanism, and a thin film of PCM melts. The results indicate that, in similar conditions, heat transfer expansion in the finned tube was higher than in the finless one. In other words, the more extended the fin surface at a constant temperature and in a given time, the higher the heat transfer rate, and the lower the melting time. In the next stage, the heat transfer mechanism converted to natural convection. In these conditions, the phase change around the heat pipe and fins was accelerated by increasing the

buoyant effects. However, the melting trend became slower due to the mitigated effects of natural convection far from the heat pipe and fins. As time passes, since the natural convection heat transfer mechanism became more dominant, the remained solid phase melted layer-wise. As presented in the aforementioned figures, the effects of the fins were prominent in the lower half of the tube, and the melting rate increased in the lower half of the absorber tube in the full fin case. To this end, liquid fraction variation over time was divided into two stages. In the first stage (0 to 22 s), the liquid fraction for the finned geometries increased linearly, and their trends almost overlapped. This result reveals that the fin geometry was the effective factor in the melting trend in the first stage. In the second stage (after 22 s), the rate of liquid fraction increment decreased gradually, and the effect of fin penetration on the liquid phase variation, especially for the finless case, was considerable. In the beginning of the process, the PCM melted around the heat pipe and fins uniformly due to the dominance of conduction heat transfer. As the melting process progressed, the convection heat transfer mechanism was amplified, and this uniform melting process was terminated. According to the presented contours, employing a full fin decreased the melting time by 87%.

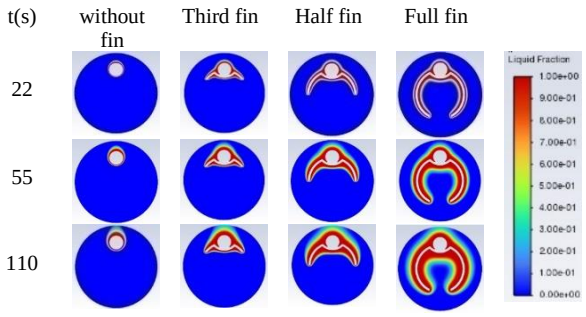

Figure 17. Partial liquid fraction range at t = 22, 55, and 110 s at 68 ˚C for four geometries.

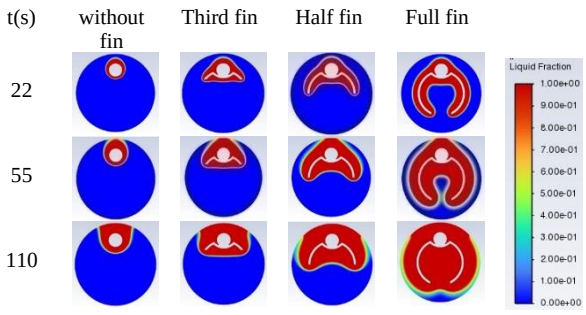

Figure 18. Partial liquid fraction range at t = 22, 55, and 110 s at 72 ˚C for four geometries.

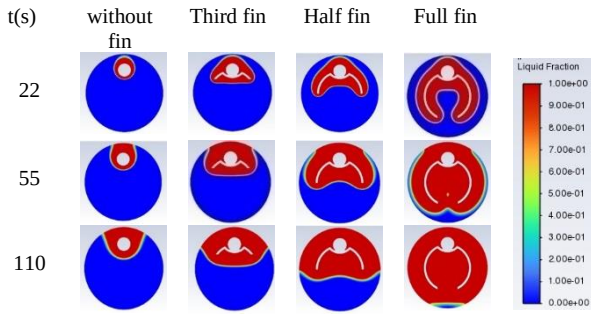

Figure 19. Partial liquid fraction range at t = 22, 55, and 110 s at 76 ˚C for four geometries.

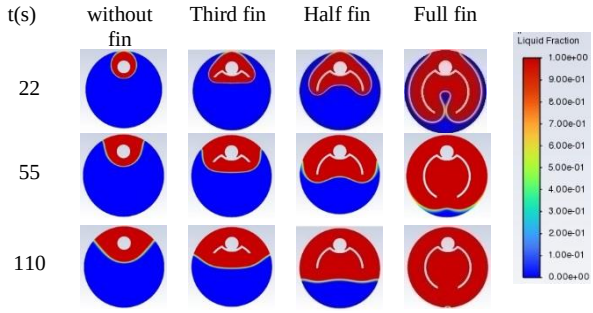

Figure 20. Partial liquid fraction range at t = 22, 55, and 110 s at 80 ˚C for four geometries.

Regarding the full fin case, it was observed that at 72 ˚C and after 110 s, the upper part of the PCM completely melted. This situation occurred at 76 ˚C after 55 s from the process beginning and at 80 ˚C after 22 s from the process beginning. However, at 80 ˚C, the PCM almost completely melted after 110 s. Regarding the half fin case, more than half of the PCM melted, and for the third fin case, less than half of the PCM melted. In the without fin case, lower than one-third of the PCM melted.

Figures 21 to 24 show the temperature variation versus time for all finned and finless cases. These figures show that temperature variation has a pattern similar to liquid fraction variation. Here, it can be observed that the effect of the fins is significant on the lower half of the collector. Therefore, the greater the fin size, the higher the PCM temperature around the fins. Therefore, the full fin has a more significant effect on the rate of PCM temperature rise due to simultaneously affecting both the lower and upper parts of the collector.

Figures 25 to 28 present the velocity patterns. It can be observed that as the surface temperature of the heat pipe and fin size increase, velocity increased due to the stronger effect of natural convection. As mentioned, for the liquid fraction and temperature results, in velocity contours at t = 110 s and for the full fin case, the velocity had the maximum value causing an increase in the melting rate of the PCM.

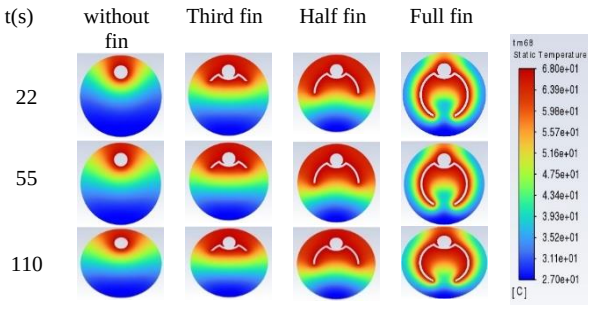

Figure 21. Partial temperature range at t = 22, 55, and 110 s at 68 ˚C for four geometries.

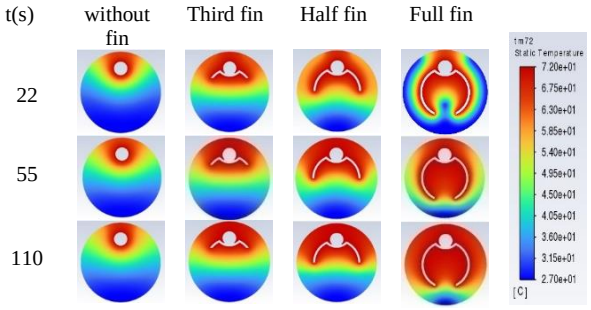

Figure 22. Partial temperature range at t = 22, 55, and 110 s at 72 ˚C for four geometries.

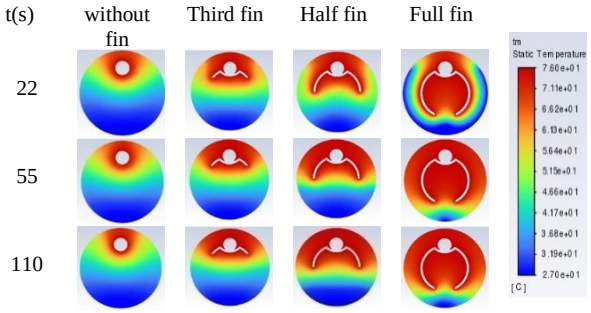

Figure 23. Partial temperature range at t = 22, 55, and 110 s at 76 ˚C for four geometries.

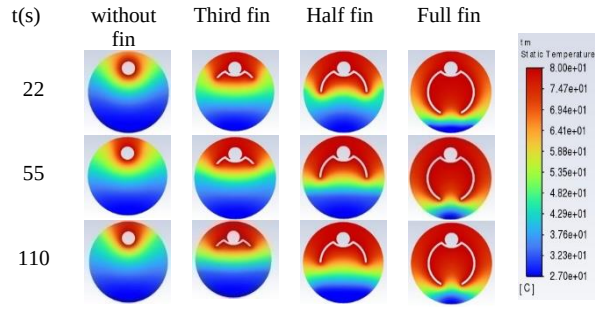

Figure 24. Partial temperature range at t = 22, 55, and 110 s at 80 ˚C for four geometries.

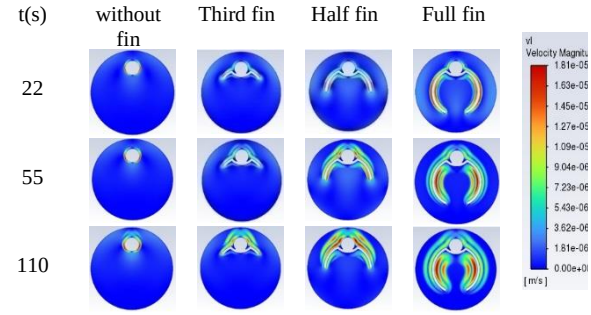

Figure 25. Velocity pattern range at t = 22, 55, and 110 s at 68 ˚C for four geometries.

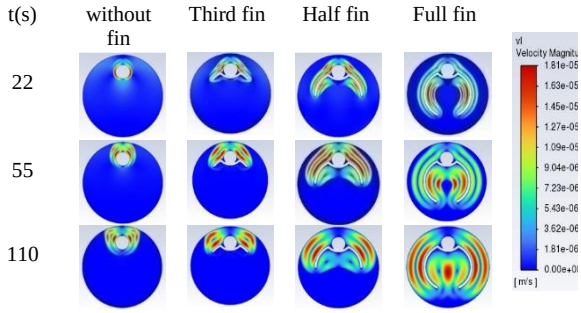

Figure 26. Velocity pattern range at t = 22, 55, and 110 s at 72 ˚C for four geometries.

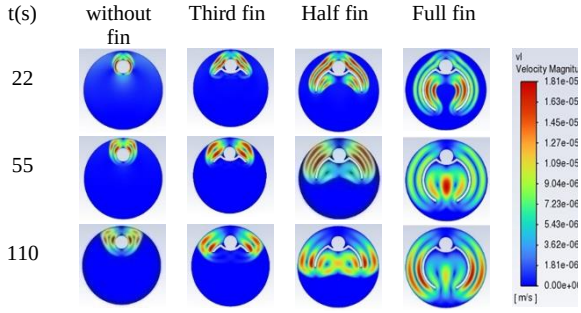

Figure 27. Velocity pattern range at t = 22, 55, and 110 s at 76 ˚C for four geometries.

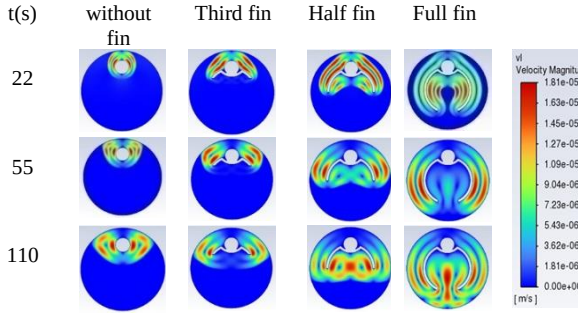

Figure 28. Velocity pattern range at t = 22, 55, and 110 s at 80 ˚C for four geometries.

7. Conclusion

This study numerically investigated the PCM melting behavior in a solar collector consisting of a heat pipe. Transient and 2D simulations were conducted for the four heat pipe cases of without fin, with a third fin, half fin, and full fin. The adiabatic tube of a solar collector was made from borosilicate glass, the heat pipe and fins were made from copper, and stearic acid was used as the PCM. The surface temperatures of the pipe and fins were considered the same. Simulations were performed for the temperatures of 68 ˚C, 72 ˚C, 76 ˚C, and 80 ˚C. The critical concluded remarks in this study are as follows:

- In comparison to the finless case, as the fin size increases, the PCM melting time decreased by 6%, 44%, and 87%, for third fin, half fin, and full fin cases, respectively.

- Variation of liquid fraction and temperature versus time for the four Stefan numbers of 0.007, 0.05, 0.09, and 0.13 (equivalent to different wall temperatures of the heat pipe) indicate an increase in the melting rate of the PCM as the Stefan number increases.
- Results show that the melting rate at the upper part of the hot surface was much higher than the lower part due to the effects of buoyancy force and natural convection.
- The effect of the fins was highlighted in the lower half of the absorber plates; the larger the fin size, the higher the melting rate of the PCM in that region, resulting in an increased melting rate.
- Contours of liquid fraction, temperature, and velocity at t = 22, 55, and 110 s indicate that assuming full fin, at 72 ˚C and after 110 s, the upper part of PCM in the collector completely melted, and a large volume of the collector space was influenced by the melting process. This situation occurred after 55 s at 76 ˚C and after 22 s at 80 ˚C.
- Contours and diagrams of liquid fraction and temperature at 0 to 22 s indicate that the liquid fraction in the presence of fins increased linearly. This result indicates that the fin was the most effective factor in the melting trend in the initial stages. After 22 s, the liquid fraction increment rate decreased gradually, and the effect of fin penetration on liquid fraction variation was considerable compared to the finless case.
- As the surface temperature of the heat pipe and fin size increased, velocity increased due to natural convection effects, and phase change occurred faster.

8. Nomenclature

Symbols		Acronyms	
A_{mush}	Plastic region constant	2D	Two-dimensional
Bo	Bond number	ETC.	Evacuated tube solar collector
C_P (kj/kg.K)	Specific heat capacity	PCM	Phase-change material
ja	Jacob or Stefan number		
H (J/g)	Sensible enthalpy		
h_s (J/g)	Latent heat of melting		
H (J/g)	Total enthalpy		
Gr_l	Grashof number		
K (W/m.K)	Thermal conductivity		
L (mm)	Length		
L_H (J/g)	Latent enthalpy		
min	minutes		
Nu_l	Nusselt number		
pr	Prandtl number		
S (s)	Second		
S	source term		
T(°C)	Liquids temperatures		
T_s (°C)	Surface temperature		
T_s (°C)	Solidus temperatures		
T_{sat} (°C)	Saturation temperature		
T_∞ (°C)	Environment temperature		

Greek letters	
B (K^{-1})	Volumetric expansion coefficient
σ (mN/m)	Surface tension
ΔH (J/g)	Latent heat
M (kg/m.s)	Dynamic viscosity
N (m^2/s)	Kinematic viscosity
P (g/cm^3)	Density
ρ_l (g/cm^3)	Liquid density
ρ_s (g/cm^3)	Solid density

9. References

[1] Golshanan, A.A.a.M.H.D., An investigation of the effect of finned inner tube eccentricity in a double-pipe heat exchanger on PCM melting time, in 29th international association of mechanical engineers in Iran, and 8th conference on the thermal power plant industry. 2021: Tehran, Iran. p. IC1128.

[2] Fuentes, E., L. Arce and J. Salom, A review of domestic hot water consumption profiles for application in systems and buildings energy performance analysis. Renewable and Sustainable Energy Reviews, 2018. 81: p. 1530-1547.

[3] Medrano, M., et al., Experimental evaluation of commercial heat exchangers for use as PCM thermal storage systems. Applied energy, 2009. 86(10): pp. 2047-2055.

[4] Huang, X., et al., Theoretical and experimental studies of impacts of heat shields on heat pipe evacuated tube solar collector. Renewable Energy, 2019. 138: pp. 999-1009.

[5] Feliński, P. and R. Sekret, Effect of PCM application inside an evacuated tube collector on the thermal performance of a domestic hot water system. Energy and Buildings, 2017. 152: p. 558-567.

[6] Abokersh, M.H. et al., On-demand operation of a compact solar water heater based on U-pipe evacuated tube solar collector combined with phase change material. Solar Energy, 2017. 155: pp. 1130-1147.

[7] Xue, H.S., Experimental investigation of a domestic solar water heater with solar collector coupled phase-change energy storage. Renewable Energy, 2016. 86: p. 257-261.

[8] Naghavi, M. et al., Theoretical model of an evacuated tube heat pipe solar collector integrated with phase change material. Energy, 2015. 91: pp. 911-924.

[9] Papadimitratos, A. et al., Evacuated tube solar collectors integrated with phase change materials. Solar Energy, 2016. 129: pp. 10-19.

[10] Feliński, P. and R. Sekret, Effect of a low cost parabolic reflector on the charging efficiency of an evacuated tube collector/storage system with a PCM. Solar Energy, 2017. 144: pp. 758-766.

[11] Li, B. and X. Zhai, Experimental investigation and theoretical analysis on a mid-temperature solar collector/storage system with composite PCM. Applied Thermal Engineering, 2017. 124: p. 34-43.

[12] Naghavi, M, et al., Thermal performance of a compact design heat pipe solar collector with latent heat storage in charging/discharging modes. Energy, 2017. 127: pp. 101-115.

[13] Essa, M.A., N.H. Mostafa, and M.M. Ibrahim, An experimental investigation of the phase change process effects on the system performance for the evacuated tube solar collectors integrated with PCMs. Energy Conversion and Management, 2018. 177: pp. 1-10.

[14] Bazri, S. et al., An analytical and comparative study of the charging and discharging processes in a latent heat thermal storage tank for solar water heater system. Solar Energy, 2019. 185: pp. 424-438.

[15] Rahimi, M. et al., Analysis of geometrical and operational parameters of PCM in a fin and tube heat exchanger. International Communications in Heat and Mass Transfer, 2014. 53: pp. 109-115.

[16] Brent, A., V.R. Voller, and K. Reid, Enthalpy-porosity technique for modeling convection-diffusion phase change: application to the melting of a pure metal. Numerical Heat Transfer, Part A Applications, 1988. 13(3): pp. 297-318.

[17] Seddegh, S., X. Wang, and A.D. Henderson, A comparative study of thermal behaviour of a horizontal and vertical shell-and-tube energy storage using phase change materials. Applied Thermal Engineering, 2016. 93: pp. 348-358.

[18] Lacroix, M., Numerical simulation of a shell-and-tube latent heat thermal energy storage unit. Solar energy, 1993. 50(4): pp. 357-367.

[19] Aghaei.A., e.a., Numerical Investigation of the Effect of Internal Tube Eccentricity on the Melting and Solidification Process of Phase Change Materials in a Double -Pipe Heat Exchanger, in third Iranian Heat and Mass Transfer Conference. Noshirvani University of Technology. 2016: Babol , Mazandaran. pp. 93: 348-358.

[20] Seeniraj, R., R. Velraj, and N. Lakshmi Narasimhan, Thermal analysis of a finned-tube LHTS module for a solar dynamic power system. Heat and mass transfer, 2002. 38(4): pp. 409-417.

[21] Dhaidan, N.S. et al., Experimental and numerical investigation of melting of NePCM inside an annular container under a constant heat flux including the effect of eccentricity. International Journal of Heat and Mass Transfer, 2013. 67: pp. 455-468.

[22] Arshad, A. et al., An experimental study of enhanced heat sinks for thermal management using n-eicosane as phase change material. Applied Thermal Engineering, 2018. 132: pp. 52-66.

[23] Rostamian, F., N. Etesami, and M. Haghgoo, Management of electronic board temperature using heat sink containing pure and microencapsulated phase change materials. International Communications in Heat and Mass Transfer, 2021. 126: p. 105407.

[24] Rahimi, M. et al., Studying the effect of radial fins on melting process of a phase change material in shell and tube heat exchanger, in 3rd National Conference on Computational and Experimental Mechanics. 2021: Tehran, Iran. pp. 635-646.

[25] Alshukri, M.J., A.A. Eidan, and S.I. Najim, Thermal performance of heat pipe evacuated tube solar collector integrated with different types of phase change materials at various location. Renewable Energy, 2021. 171: pp. 635-646.

[26] Zhu, C. et al., Air-Type Vacuum-Tube Solar Collector Design and Heat Collection Performance Test. Energies, 2022. 15(15): p. 5679.

[27] Elbrashy, A. et al., Experimental study of solar air heater performance with evacuated tubes connected in series and involving nano-copper oxide/paraffin wax as thermal storage enhancer. Environmental Science and Pollution Research, 2023. 30(2): pp. 4603-4616.

[28] Kharkeshi, B.A. et al., Experimental study of an oscillating water column converter to optimize non-linear PTO using genetic algorithm. Energy, 2022: p. 124925.

[29] Bergman, T.L. et al., Introduction to heat transfer. 2011: John Wiley & Sons.

[30] Chopra, K. et al., Thermal performance of phase change material integrated heat pipe evacuated tube solar collector system: An experimental assessment. Energy Conversion and Management, 2020. 203: p. 112205.

[31] Nematpour Keshtali, A.a.M.S., Numerical investigation of nano PCM melting inside the triangular compartment, in Mechanical engineering

journal of Amirkabir university. 2020: Tehran, Iran. pp. 52: 250-252.

[32] Hamit, A. and M.Ş. Adin, Numerical analysis of damaged helical gear wheel. Batman Üniversitesi Yaşam Bilimleri Dergisi, 2021. 11(1): p. 43-56.

[33] Hamit, A., R.K. Ergün, and M.Ş. Adin, Computer aided numerical damage analysis of the axle shaft. European Mechanical Science, 2022. 6(3): pp. 201-206.

[34] Tan, F. et al., Experimental and computational study of constrained melting of phase change materials (PCM) inside a spherical capsule. International Journal of Heat and Mass Transfer, 2009. 52(15-16): pp. 3464-3472.